Check for updates

CLIMATOLOGY

The pace of meeting carbon emission targets alters regional climate risks

In-Hong Park[1], Sang-Wook Yeh[2]*, Andrew D. King[3,4]

Copyright © 2026 The Authors, some rights reserved; exclusive licensee American Association for the Advancement of Science. No claim to original U.S. Government Works. Distributed under a Creative Commons Attribution NonCommercial License 4.0 (CC BY-NC).

Carbon budgets, derived from the near-linear link between cumulative carbon emissions and global warming, guide climate mitigation and adaptation. However, the impact of the pace of reaching a target budget on climate response remains uncertain. Using 29 climate models, we compare scenarios reaching the same carbon emission target slowly or quickly. A faster trajectory produces stronger land warming and greater exposure to extreme heat waves than a slower pathway. Of 46 land regions, 37 (80%) warm more and 39 (85%) experience higher heat wave exposure in the faster case. This arises because the deep ocean cannot absorb heat rapidly, amplifying atmospheric warming. These findings underscore that not only the total emissions but also the pace of emissions critically governs regional climate risks.

INTRODUCTION

The proportional relationship between cumulative anthropogenic CO_2 emissions and global warming since preindustrial periods has substantially contributed to the development of future climate change mitigation and adaptation policies (*1*–*3*). This framework provides a foundation for calculating the total carbon budgets required to meet the goals of the Paris Agreement—limiting global warming to well below 2°C, and ideally 1.5°C, above preindustrial levels (*4*, *5*). It has also encouraged many countries to commit to net-zero pledges (*6*, *7*) and supports strong mitigation pathways, including CO_2 removal and overshoot scenarios (*8*, *9*). However, as components of the Earth system respond to external forcing on varying timescales (*10*, *11*), it is crucial to understand their changes under different carbon emission rates for practical climate policies (*12*).

The latest Climate Model Intercomparison Project phase 6 (CMIP6) global climate models (GCMs) simulate that the magnitude of global-mean surface temperature (GMST) rise is consistent with the corresponding carbon budget regardless of future scenarios (*13*). However, the pace of reaching the target carbon budget—whether slowly or quickly—can affect regional climate change and associated risks. At the same time, regional climate responses remain uncertain (*14*, *15*). To date, different warming trajectories, such as transient versus equilibrium climate states, have been examined to understand how the pace of reaching a warming goal influences regional impacts (*16*, *17*). Stronger land warming and extremes have been found under transient pathways, often attributed to delayed surface ocean adjustment. However, most of these findings stem from single model analyses or idealized experiments focused on fixed warming targets (*18*, *19*) without accounting for intermodel differences in cumulative emissions. This limitation reduces their relevance to real-world policy decisions. These gaps underscore the need for research grounded in cumulative carbon budgets that incorporate both the pace and pathways of emissions—frameworks central to the Paris Agreement and climate mitigation policies—and are critical for informing effective mitigation and adaptation strategies.

Variation in the response of Earth system components, such as the extent of sea ice melting (*20*) and changes in ocean circulation (*21*), to the same carbon budget may lead to substantial regional differences even at the same global warming level. These differences influence extreme climate events like heat waves, which are highly sensitive to local climatic conditions and feedbacks (*22*). While the link between the CO_2 concentration and the frequency and intensity of extreme events is well established (*23*–*27*), how these responses vary with the timing of reaching the target temperature remains uncertain. Understanding how extreme climate events respond to different emission pathways is particularly important, as their regional impacts are amplified by vulnerabilities such as population demographics and health infrastructure (*28*). Therefore, considering the pace of emissions is essential for improving climate risk assessments and developing effective mitigation and adaptation strategies.

Here, on the basis of the framework of similar GMST for the same carbon budget (*13*), we compare the response of the climate system to reaching the target carbon budget, corresponding to the Paris Agreement's warming target, at different paces, either slow or fast, using 29 CMIP6 GCMs. Using different shared socioeconomic pathway (SSP) emission scenarios (*29*), we compare a slow scenario (i.e., SSP1-2.6) with a fast scenario (i.e., SSP5-8.5) for reaching the target carbon budget. We find that extremely hot temperatures are more intense and that a larger area is exposed to extreme heat waves in the fast scenario than in the slow scenario.

RESULTS

GMST changes and regional differences

We analyze the relationship between cumulative carbon emissions (CCEs hereafter) and GMST under different future scenarios for the SSP1-2.6 and the SSP5-8.5 carbon emission scenarios using 29 CMIP6 GCMs (Fig. 1A). Both CCEs and GMST are averaged over 30 years to reduce the influence of internal variability (*30*). To calculate CCEs, we apply a proxy method that combines atmospheric CO_2 concentration, carbon uptake by the ocean and on land, and land-use change resulting from the limited availability of scenarios and GCMs that provide direct carbon emission values (see Materials and Methods) (*31*).

While the magnitude of the change in GMST relative to CCEs varies considerably between the GCMs because of differences in climate

[1]Department of Civil and Environmental Engineering, Konkuk University, Seoul 05029, Republic of Korea. [2]Department of Climate and Energy Systems Engineering, Ewha Womans University, Seoul, South Korea. [3]School of Geography, Earth and Atmospheric Sciences, University of Melbourne, Parkville, VIC, Australia. [4]ARC Centre of Excellence for the Weather of the 21st Century, Parkville, VIC, Australia.
*Corresponding author. Email: swyeh@ewha.ac.kr

Downloaded from https://www.science.org at EWHA Womans University on September 30, 2026

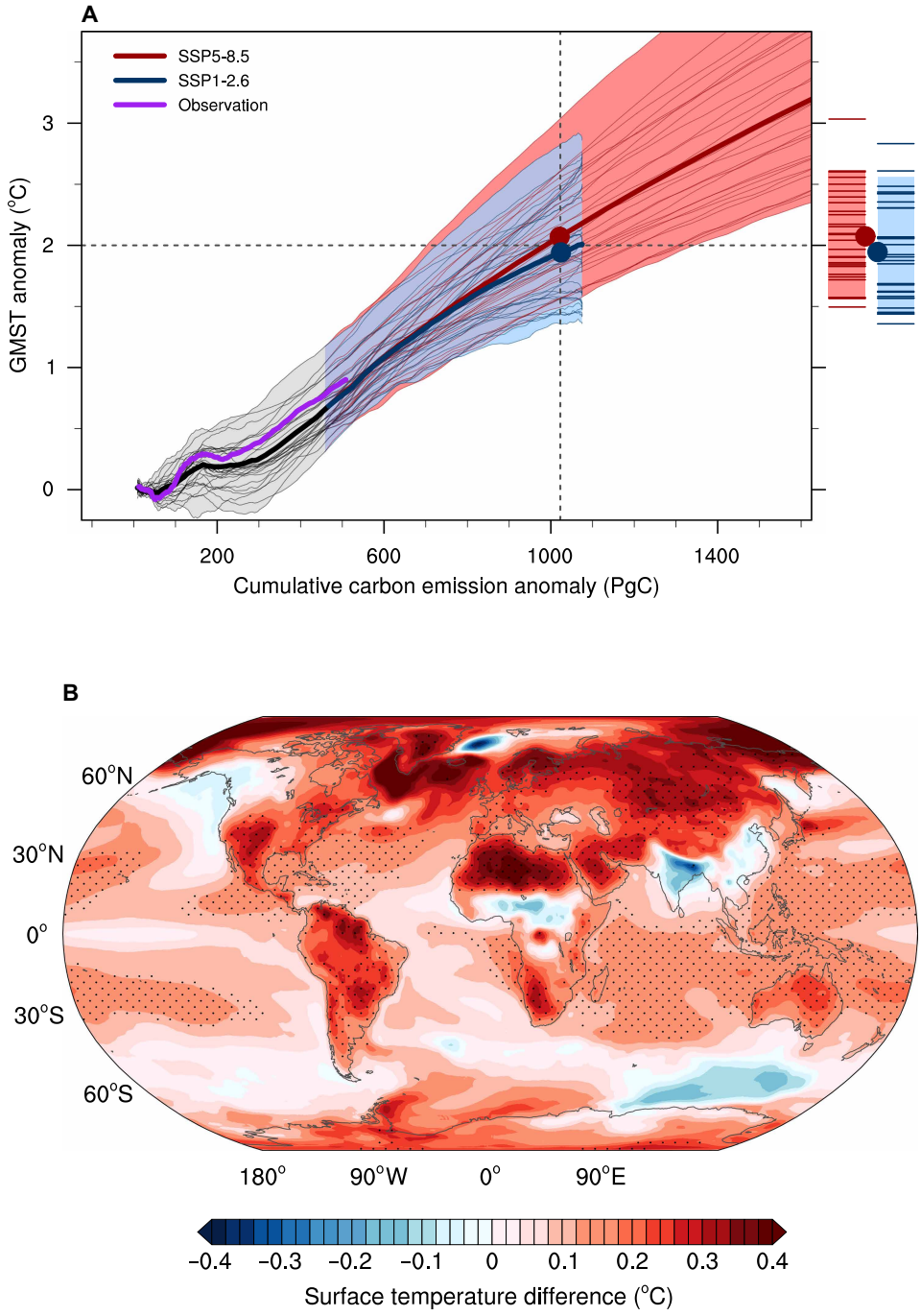


Fig. 1. Response of GMST to CCEs and regional warming differences between slow and fast scenarios. (**A**) GMST anomaly relative to the preindustrial period (1850 to 1900) and CCEs since 1850. Black lines indicate the historical period (1850 to 2014), while colored lines indicate future scenarios (blue: SSP1-2.6; red: SSP5-8.5). Thin lines indicate individual results from 29 CMIP6 Earth System Models (GCMs), and thick lines indicate the MME. The shading indicates the range (maximum to minimum GMST) among 29 GCMs based on the MME of CCEs. The purple line represents observations from the Global Carbon Project (*44*) and HadCRUT5 (*45*). All variables are averaged over 30 years to minimize internal variability, and the markers indicate the slow scenario period (2045 to 2074 in SSP1-2.6) and the fast scenario period (2026 to 2055 in SSP5-8.5). The bar plot on the right compares the GMST when the target CCEs are reached. The shading represents the 5th to 95th percentiles, the horizontal lines indicate individual GCMs, and the markers represent the MME. (**B**) Spatial distribution of differences in surface mean temperature between the fast and slow scenarios. Stipples indicate regions where the differences are statistically significant based on a paired *t* test, confirmed by a bootstrap test.

Downloaded from https://www.science.org at EWHA Womans University on September 30, 2026

sensitivity (*32*, *33*), each GCM (colored thin lines in Fig. 1A) shows an approximately linear relationship between CCEs and GMST in both SSP1-2.6 and SSP5-8.5, excluding the historical period influenced by internal variability and aerosol effects (*34*). The multimodel mean (MME) (thick lines in Fig. 1A) reproduces the observed linear relationship between CCEs and GMST well regardless of the scenarios. To examine the pace of reaching the target CCEs, we selected two periods when the difference in CCEs between the two scenarios was minimized and the MME GMST approached the Paris Agreement upper warming level of 2.0°C relative to the preindustrial period: 2045 to 2074 for SSP1-2.6 and 2026 to 2055 for SSP5-8.5 (see Materials and Methods and fig. S1A). Thus, the SSP1-2.6 scenario reaches the target CCEs later (slow scenario hereafter), whereas the SSP5-8.5 scenario reaches them early (fast scenario hereafter). The MMEs of CCEs in the two scenarios are comparable, with 1024 PgC in the slow scenario and 1021 PgC in the fast scenario. In addition, the CCEs of each GCM are close to the 1:1 line between the two scenarios, indicating that the difference in CCEs between the fast and slow scenarios is negligible (fig. S1B). Therefore, although specific time periods have been chosen, the similarity of CCEs across different scenarios within each GCM suggests that this time selection is suitable for assessing Earth system responses to differences in the timing of reaching the target carbon budget.

The GMST MME change is 2.07°C in the fast scenario, which is slightly higher than 1.94°C in the slow scenario. The change in GMST was higher in the fast scenario than in the slow scenario in 86% (25 of 29) of GCMs (fig. S2A). However, the intermodel standard deviations (0.38° and 0.41°C, respectively) exceed the differences between the scenarios. The results of a bootstrap test accounting for model uncertainty (see Materials and Methods) (*35*) indicate that the difference in GMST between the two scenarios is not statistically significant, as the difference between the two scenario means is smaller than the sum of the standard deviations between models (fig. S2B). A similar pattern is also found in the results using the 14 GCMs that provide all variables related to CCEs (fig. S2, C and D). Although there is a consistent difference in GMST within each GCM, model uncertainties make the overall difference in GMST between scenarios statistically insignificant.

Meanwhile, the spatial distribution of surface temperature differences between the fast and slow scenarios when reaching target CCEs with different timing reveals regionally statistically significant patterns (Fig. 1B). These contrasts emerge despite the nonsignificant difference in GMST. The surface mean temperature difference between the two scenarios, calculated as the fast scenario minus the slow scenario, shows stronger warming over most land areas. In low-latitude regions near the equator, including Central America and North Africa, these differences are statistically significant, as determined by the bootstrap test (figs. S3 and S4A). Moreover, these differences are not limited to surface mean temperature but extend to maximum and minimum temperatures, with the fast scenario projecting higher values over land compared to the slow scenario (fig. S4, B and C). This suggests that the slow or fast pace of reaching target CCEs may play a role in driving regional climate differences. In particular, a slow approach to the target CCEs tends to mitigate warming over land areas, and thus human exposure, while a fast emission pathway leads to more warming in these areas.

Extreme temperature and heat wave differences

To examine the influence of the different timing of reaching the CCE target on extreme climate events, we analyzed the extreme heat events, defined as the annual maximum of the daily maximum temperature (TXx hereafter) (*36*). Compared to the preindustrial period (1850 to 1900), the global land mean TXx increases in both scenarios (Fig. 2A). The global-mean TXx change in the fast scenario reaches 2.66°C, which is greater than the 2.46°C TXx warming in the slow scenario. Among the 29 GCMs, 79% (23 models) showed a greater increase in global land TXx in the fast scenario than in the slow scenario. The bootstrap test showed that the standard deviation in both scenarios was 0.1°C, while the mean difference was ~0.2°C (fig. S5A). On a global scale, the occurrence of extreme events is statistically significantly different for the same CCEs depending on when the CCE target is reached. However, at regional scales, these differences may not always be statistically significant because of internal climate variability and model uncertainty.

Meanwhile, the consensus of GCMs on the difference in the land area exposed to extreme heat waves is higher than that on the global land TXx mean difference (Fig. 2B). Among the 29 GCMs, 86% (25 GCMs) indicate that a larger land area will be exposed to extreme heat waves in the fast scenario (MME of 35.7%) than in the slow scenario (31.7%). This difference is statistically significant in the bootstrap test (fig. S5B). This indicates that there is high confidence that more land regions would experience extreme heat waves in the fast scenario (where the target CCEs are reached more quickly) than in the slow scenario (where the target CCEs are reached later), even under similar GMST conditions (Fig. 1A). Note that extreme heat wave exposure is defined as events exceeding the 99th percentile intensity of the historical period from 1850 to 2014 (Materials and Methods) (*37*, *38*).

Furthermore, we repeated the analysis using 30-year periods centered on when each model reaches a CCE level of 1000 PgC and when each model reaches 2°C global warming. Across these alternative definitions, most models consistently show larger increases in TXx and greater exposed land area to extreme heat waves under the fast pathway than under the slow pathway, indicating that the identified pace-dependent differences are robust at the individual-model level (fig. S6).

Results for the moderate pathway (SSP2-4.5) consistently fall between those for the slow (SSP1-2.6) and fast (SSP5-8.5) pathways for global TXx and extreme heat wave exposure at similar CCEs (defined for SSP2-4.5 as the 30-year window of 2033 to 2062 with multimodel-mean CCEs matched to the slow/fast scenarios). In 23 of 27 GCMs (85%), both the global-mean TXx and land area exposed to extreme heat waves are lower than in the fast pathway, reinforcing the robustness of the pace-dependent effect across GCMs and scenarios (fig. S7).

In addition to TXx and exposed land area to extreme heat waves, we examined the frequency of extreme heat wave occurrences, another impact-relevant metric. Consistent with the results for exposed land area to extreme heat waves (see Fig. 2B), the global land-mean frequency of extreme heat wave occurrences is higher under the fast scenario than under the slow scenario for the same CCEs (fig. S8).

Regionally, the difference between the two scenarios of TXx and extreme heat wave exposure is more substantial (Fig. 3). Among the total 46 land subregions defined by the Intergovernmental Panel on Climate Change (IPCC) Sixth Assessment Report (AR6) Working Group I (WG I) reference regions (fig. S3), 37 regions (about 80%) show greater changes in TXx in the fast scenario compared to the slow scenario, with GCM agreement exceeding 60% (Fig. 3A). In

Downloaded from https://www.science.org at EWHA Womans University on September 30, 2026

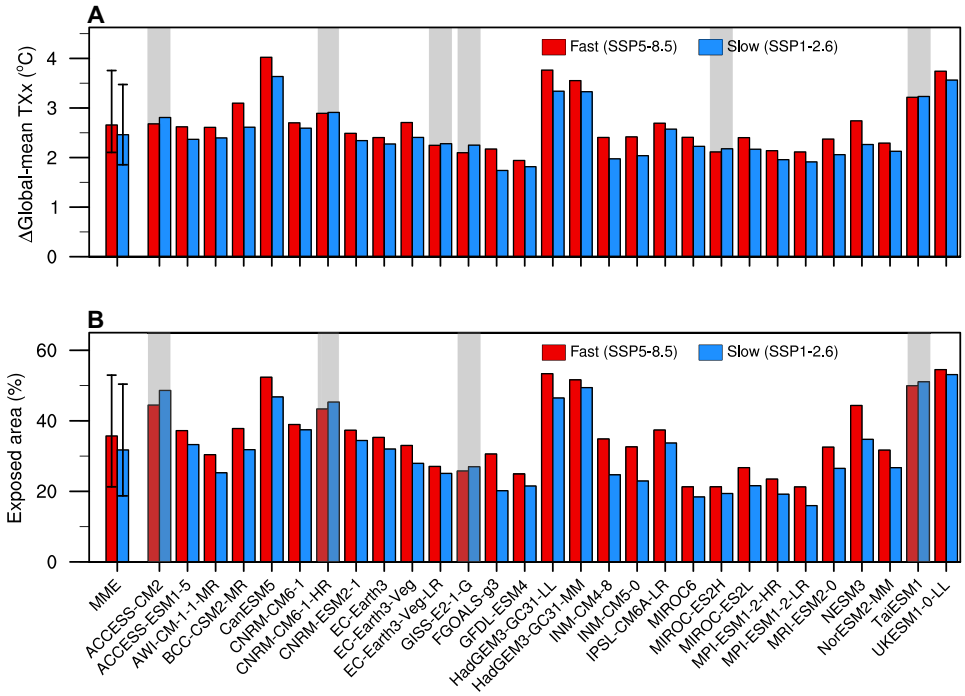


Fig. 2. Difference in global temperature extremes between the fast and slow scenarios. (**A**) Comparison of global-mean TXx changes in the slow (SSP1-2.6, blue) and the fast (SSP5-8.5, red) scenarios across 29 GCMs. In 23 of 29 GCMs (79%), the increase in global-mean TXx is greater in the fast scenario than in the slow scenario. The six GCMs that simulate a larger increase in TXx in the slow scenario are shown in gray. Error bars in the MME represent the 95% confidence interval. (**B**) Land area exposed to extreme heat waves.

particular, the Mediterranean, Sahara, South America, and Arabian Peninsula regions exhibit statistically significant differences using the bootstrap test. In addition, when the difference in extreme heat wave exposure was calculated as the fast scenario minus the slow scenario, positive values were obtained in all but 7 of the 46 IPCC subregions, meaning that most regions experience higher exposure under the fast pathway, with GCM agreement on the sign of the change exceeding 60% (Fig. 3B). The high level of agreement among GCMs indicates that more land areas were exposed to extreme heat waves in the fast scenario compared to the slow scenario. Regional exposure ratios, calculated as the percentage of grids exposed to extreme heat waves relative to total land grids in each region, were consistent with the global exposure calculation. All regions except South Asia (SAS), Africa, South Australia, and Western Antarctica, exhibit positive values. In particular, 22 of the 46 total subregions (48%) showed statistical significance by passing the bootstrap test.

While the difference in GMST between the fast and slow scenarios is not statistically significant, climate risks including extreme heat wave exposure are more pronounced in the fast scenario. This suggests that delaying the timing of reaching the target CCEs by slowing the pace of emissions can help significantly reduce regional climate risks such as extreme heat waves.

Physical mechanisms for reduced climate risks by delaying carbon emission targets

To understand the differences in TXx and extreme heat wave exposure, despite similar GMST changes in both scenarios, we compared the oceanic responses in the two scenarios relative to the change in CCEs. While the ocean heat content (OHC) increases linearly with increasing CCEs in the fast scenario, the slow scenario shows a nonlinear relationship: OHC increases nonlinearly with increasing CCEs (Fig. 4A). Consequently, by the time the target CCE is reached, the slow scenario has a larger OHC than the fast scenario, indicating that more heat is stored in the ocean in the slow scenario. The deep ocean warms more slowly in response to greenhouse gas increases because of its high thermal inertia and slow heat transport (*39*, *40*). Consequently, the deep ocean continues to warm even without sustained CO_2 forcing. Moreover, in contrast to the GMST, the difference in OHC between the two scenarios is statistically significant based on the bootstrap test (fig. S9).

The global OHC difference (the fast scenario minus the slow scenario) shows negative values over most oceans, with pronounced differences in the Atlantic and Arctic regions (Fig. 4B). Approximately 90% of the energy imbalance caused by anthropogenic greenhouse gas emissions is absorbed by the oceans (*41*), leading to differences in atmospheric energy between scenarios because of associated variations in OHC. Consistent with enhanced ocean heat uptake under the slow scenario, the zonal-mean ocean temperature difference reveals a distinct vertical structure, with temperature differences between the fast and slow scenarios most pronounced in the upper ocean (Fig. 4C). This indicates that differences in heat storage associated with the pace of emissions are primarily expressed below the surface, while surface warming—and, hence, potential differences in marine heat wave characteristics—may differ between the fast and slow scenarios. In contrast to the global OHC difference, the zonal-mean atmospheric temperature difference shows positive values over most

Downloaded from https://www.science.org at EWHA Womans University on September 30, 2026

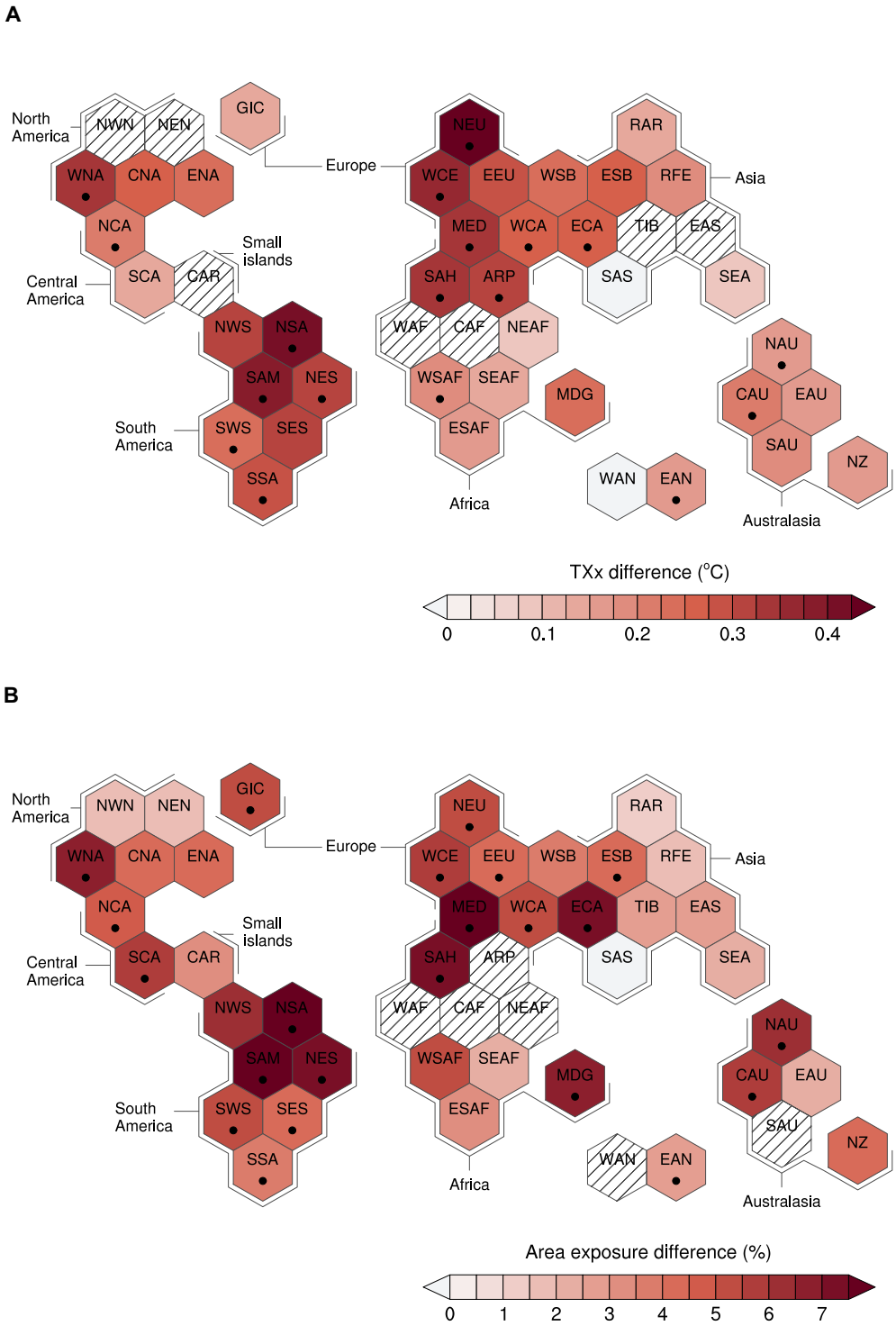


Fig. 3. Differences in the spatial distribution of extremely hot events based on the timing of reaching the target CCEs. (**A**) Difference between the fast and slow scenarios (fast minus slow) in TXx across the 46 IPCC AR6 reference regions. (**B**) Same as (A) but for extreme heat wave exposure. The filled color of each hexagon represents the difference, while a dot indicates regions where the difference between scenarios is statistically significant based on a paired *t* test, confirmed by a bootstrap test. Hatched hexagons indicate regions where the sign of the difference between GCMs is consistent in less than 60% of GCMs (less than 18 of 29 GCMs).

Downloaded from https://www.science.org at EWHA Womans University on September 30, 2026

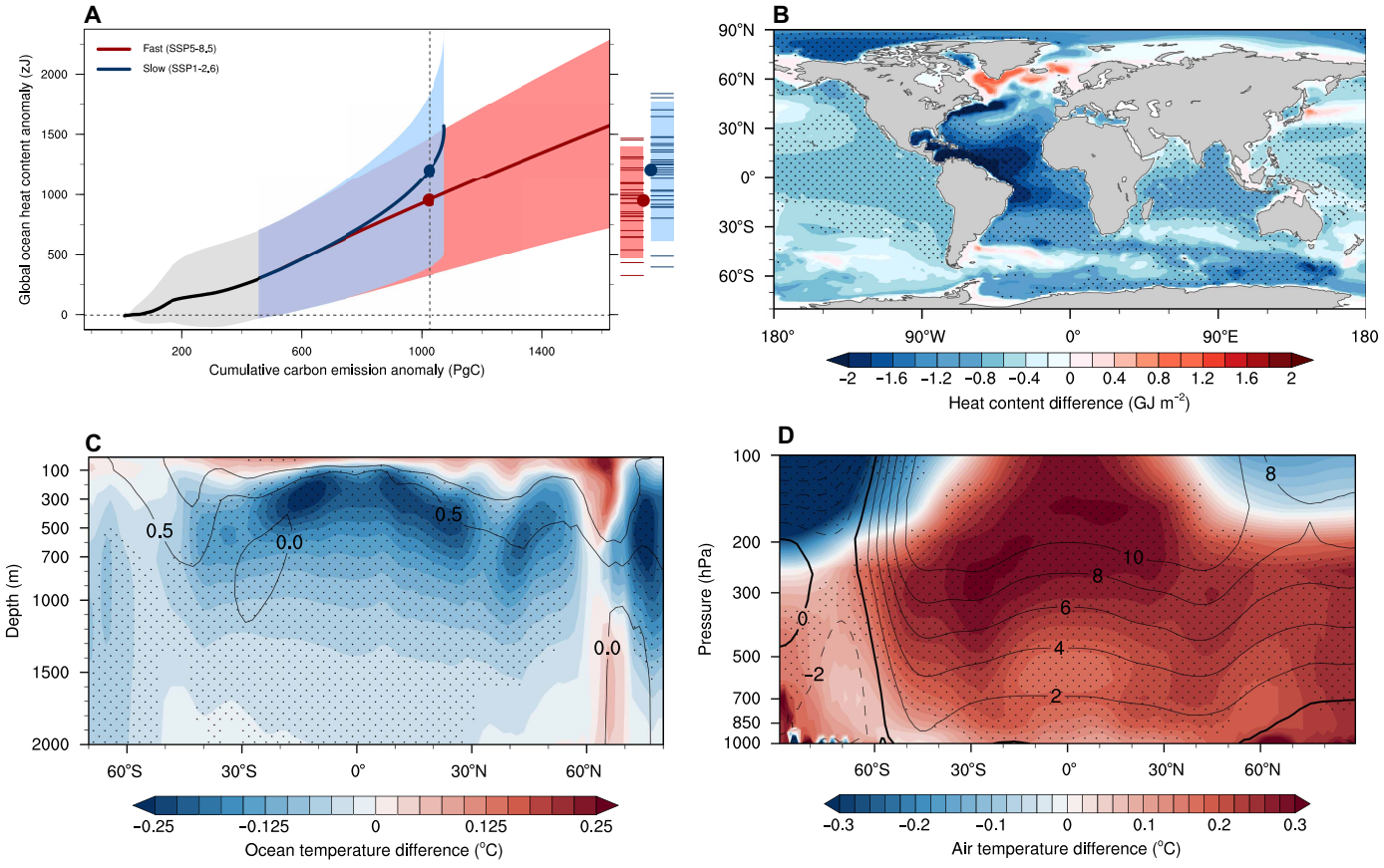


Fig. 4. Differences in the ocean and atmosphere based on the timing of reaching the target CCEs. (**A**) Relationship between CCEs and global OHC for SSP1-2.6 (blue) and SSP5-8.5 (red) scenarios. Thick lines represent the MME, and the shading indicates the maximum and minimum OHC values among 29 GCMs on the basis of the MME of CCEs. Markers indicate the slow scenario period (2045 to 2074 in SSP1-2.6) and the fast scenario period (2026 to 2055 in SSP5-8.5). (**B**) Spatial distribution of OHC differences (the fast scenario minus the slow scenario). Stipples indicate regions where the differences between the two scenarios are statistically significant by the bootstrap test. (**C**) Zonal-mean ocean temperature differences (the fast scenario minus the slow scenario). Contours indicate ocean temperature changes in the fast scenario relative to the preindustrial period. (**D**) Zonal-mean atmospheric temperature differences (the fast scenario minus the slow scenario). Contours indicate differences in geopotential heights, and stipples indicate regions where the differences are statistically significant based on a paired *t* test, confirmed by a bootstrap test.

latitudes and altitudes (Fig. 4D). This indicates that although the GMST differences are small (Fig. 1), atmospheric warming is more pronounced in the fast scenario than in the slow scenario. The difference in geopotential height at each pressure level also shows positive values in most regions (contours in Fig. 4D), supporting the notion that warming through the troposphere is stronger in the fast scenario than in the slow scenario. The greater energy retained in the atmosphere in the fast scenario increases the likelihood of exposure to extreme heat waves. In summary, despite similar CCEs and GMST, slow reaching of target CCEs leads to larger OHC and reduced atmospheric warming, whereas fast reaching of target CCEs results in more pronounced atmospheric warming and greater energy retention in the atmosphere.

DISCUSSION

Our results highlight that the pace of reaching CCEs significantly alters regional climate risks, in particular exposure to extreme heat waves. Although GMST responds linearly to CCEs, our results indicate that the fast reaching of target CCEs, i.e., a rapid CO_2 release pathway, leads to greater land warming and increased exposure to extreme heat wave events. This is because less heat is stored in the ocean in the fast scenario, amplifying atmospheric warming and increasing the risk of extreme heat waves. These findings challenge the conventional assumption that only total cumulative emissions matter and emphasize the need to consider emission pathways when designing mitigation and adaptation strategies.

Differences in non-CO_2 forcing, particularly aerosols, represent an additional factor that can modulate regional temperature responses when comparing emission scenarios. Using a fine particulate matter ($PM_{2.5}$)–based assessment (see Materials and Methods) (*42*), we find that aerosol burdens are higher under the fast scenario than under the slow scenarios over regions with historically high aerosol loading, particularly SAS, Southeast Asia (SEA), and parts of East Asia (EAS) (fig. S10). Elevated aerosol concentrations reduce incoming solar radiation and can therefore dampen surface warming locally. Consistently, the fast scenario exhibits weaker warming or local cooling over parts of SAS, SEA, and EAS compared with the slow scenario (Fig. 1B). Despite the fact that the regions with pronounced aerosol differences (SAS, SEA, and EAS) are excluded, however, the difference in GMST between the fast and slow scenarios remains statistically insignificant (fig. S2). This indicates that while aerosol forcing can locally modulate

Downloaded from https://www.science.org at EWHA Womans University on September 30, 2026

regional temperature responses, it hardly affects the global-scale temperature contrast between the fast and slow scenarios. Nevertheless, aerosol forcing plays an important role in shaping regional extreme temperature and heat wave exposure responses, particularly over aerosol-rich regions including SAS, SEA, and EAS (Fig. 3).

To further assess the sensitivity to the warming threshold—particularly in light of evidence that aerosol reductions can exert a strong influence on near-term warming and climate extremes (*43*)—we conducted complementary analyses anchored at multiple warming levels between 1.5° and 1.9°C above preindustrial conditions (figs. S11 and S12). Across these alternative thresholds, the global-scale responses remain qualitatively consistent. Differences in GMST between the fast and slow scenarios remain small, while from 1.6°C of global warming onward, the fast scenario systematically exhibits larger increases in global land-mean TXx and greater land area exposed to extreme heat waves. The sign of the fast versus slow contrast does not reverse across the tested warming levels, indicating that the identified pace-dependent differences are not an artifact of the specific 2°C threshold choice. Together, these sensitivity tests demonstrate that while aerosol forcing may modulate near-term and regional climate responses, the main global-scale conclusions of this study remain robust across a range of warming thresholds.

Beyond aerosol-rich regions, some areas exhibit weaker warming in the fast scenarios than the slow scenario, including the northeastern Pacific and parts of the Southern Ocean. To investigate the origin of these regional signals, we analyzed large-ensemble simulations from two single-model ensembles, ACCESS-ESM1-5 and CanESM5, both of which are included in our 29-model ensemble and consistently exhibit stronger global-mean TXx and larger exposed areas to extreme heat waves in the fast scenario than in the slow scenario. While the ensemble-mean fast-minus-slow surface temperature differences in these regions indicate cooling, this signal is accompanied by substantial internal variability, resulting in a low signal-to-noise ratio (fig. S13). This suggests that the cooling anomalies in the northeastern Pacific and Southern Ocean do not represent robust forced responses but instead arise predominantly from internal climate variability and regional ocean-atmosphere dynamics.

While differences between transient and stabilizing climates have been identified before, here, we find significant differences in climate means and extremes within the 21st century because of the pace of emissions and associated global warming. Plausible emission reduction pathways can reduce temperature-related climate hazards with benefits to current generations. Our findings add further evidence showing the large and wide-ranging benefits to rapid emission reductions. Our analysis shows that a distinct pattern of difference already emerges within the 21st century, rather than only at end-of-century horizons. These findings highlight that the pace of emissions influences climate risks on near-term timescales, making the choice of emission pathway directly relevant for current generations.

Our results also have implications for climate policy and the carbon budget. Current frameworks for climate mitigation, including the Paris Agreement, are primarily based on limiting cumulative emissions to achieve temperature targets (e.g., 1.5° or 2°C). However, our findings suggest that the rate of emissions also needs to be considered (*12*), as fast emissions could lead to increased regional climate risks, particularly for heat-sensitive regions such as North Africa, the Middle East, and parts of South America. Furthermore, our findings suggest that climate risk assessments should integrate emissions pathway considerations, rather than focusing solely on temperature targets. Policy-makers should integrate emission pathways into climate strategies to minimize regional disparities in climate impacts and ensure that mitigation efforts are aligned with sustainable and equitable adaptation measures.

MATERIALS AND METHODS

Earth system models and observational datasets

We used 29 GCMs to calculate climate variables associated with the different timings of reaching the target CCEs and 14 models to calculate CCEs in CMIP6 for the historical run (1850 to 2014) and all projections based on SSP concentration scenarios (2015 to 2100) (*29*). The model names and modeling groups are given in table S1. To minimize the influence of internal variability, a 30-year running average was used for each scenario, and all anomalies were calculated relative to the preindustrial period (1850 to 1900). For extreme variables (annual maximum of the daily maximum temperature and heat wave exposure), the original grid resolution was used, whereas other climate variables were interpolated to a 1° by 1° grid. Observational data for carbon emissions were obtained from the Global Carbon Project (*44*), and HadCRUT5 (*45*) was used for observed GMST.

CCE calculation

We use 14 CMIP6 GCMs, which provide the necessary land-atmosphere and ocean-atmosphere CO_2 fluxes. This allows GCMs with comparable concentration scenarios and includes climate-carbon cycle interactions. To maintain consistency with the prescribed CO_2 runs for heat wave exposure and other climate change variables, we use the historical runs (with prescribed atmospheric CO_2) rather than the esm-hist runs (which interactively calculate atmospheric CO_2 on the basis of prescribed CO_2 emissions). The interactive response of modeled land and ocean carbon sinks to changes in climate and atmospheric CO_2 enables the emissions corresponding to each scenario to be diagnosed for each GCM (*31*). The cumulative global fossil fuel CO_2 emissions (E_{ff}) associated with each scenario are determined by the atmospheric carbon content changes (ΔC_A) driven by the prescribed atmospheric CO_2 levels, alongside simulated changes in global ocean carbon storage (ΔC_O) and land carbon storage (ΔC_L)

$$E_{ff}(t) = \Delta C_A(t) + \Delta C_O(t) + \Delta C_L(t) \quad (1)$$

The equivalent prescribed increase in atmospheric carbon is calculated as

$$\Delta C_A(N) = 2.12\left[co_2(N) - co_2(1850)\right] \quad (2)$$

where $co_2(N)$ is the annual-mean, global-mean CO_2 concentration for year N in ppmv (parts per million by volume), and 2.12 is the usual conversion factor from ppmv to PgC.

To estimate the carbon sink storage, time series of net biome productivity over land (CMIP variable: nbp) and ocean CO_2 flux (CMIP variable: fgco2) was calculated from monthly spatial fields. For the models, we calculate the carbon store changes (PgC) for land and ocean, for each year N, as the sum of the annual-mean fluxes

$$\Delta C_O(N) = \sum_{y=1850}^{y=N} \mathrm{fgco2}(y) \quad (3)$$

$$\Delta C_L(N) = \sum_{y=1850}^{y=N} \mathrm{nbp}(y) \quad (4)$$

Downloaded from https://www.science.org at EWHA Womans University on September 30, 2026

where fgco2(y) is the annual-mean, global total ocean CO_2 flux (PgC year^{-1}), and nbp(y) is the annual-mean, global total net ecosystem productivity over land (PgC year^{-1}).

We calculate the terms in this equation relative to 1850. To convert E_{ff} into the total cumulative emissions (E), adding on the cumulative global net land-use emissions associated with each SSP scenario is essential. Some GCMs provide net land-use change emissions interactively (*46*), but the number of GCMs with this information is limited. Therefore, we use prescribing the standard net land-use changes (E_{lu}) associated with each SSP scenario following previous study

$$E(t) = \Delta C_A(t) + \Delta C_O(t) + \Delta C_L(t) + E_{lu}(t) \quad (5)$$

Definition of slow and fast scenarios

To identify the impact of the timing of reaching target CCEs, we selected two distinct periods: one representing slower progress resulting from rapid climate action based on SSP1-2.6 (slow scenario) and the other representing fast progress resulting from slow climate action based on SSP5-8.5 (fast scenario). CCEs were calculated using the MME, given the limited number of GCMs providing all flux variables required for emission calculations and the differing biases among GCMs. For the slow scenario (SSP1-2.6), the selected period is 2045 to 2074, and for the fast scenario (SSP5-8.5), it is 2026 to 2055, maintaining a 19-year time interval between the two scenarios (*47*). There are some regional differences in aerosol concentrations between the scenarios and periods, and this may contribute to regional uncertainties. When the target was reached, the CCEs at the slow scenario (SSP1-2.6) were 1024 PgC, slightly larger than 1021 PgC in the fast scenario (SSP5-8.5). To test robustness, we also analyzed a moderate pathway using SSP2-4.5 (2033 to 2062). For TXx and heat wave exposure, 27 GCMs provided SSP2-4.5 daily fields; HadGEM3-GC31-MM and CNRM-CM6-1-HR lacked SSP2-4.5 and were excluded.

Definition of extreme climate events

The extremely high temperature is calculated as the annual maximum of the TXx, following the definition of the ETCCDI (Expert Team on Climate Change Detection and Indices) (*36*). The anomaly of TXx was calculated as the change from the preindustrial period mean (1850 to 1900). To evaluate extreme heat events, we applied the heat wave magnitude index daily (HWMId) (*48*). HWMId defines a heat wave as a period of at least three consecutive days with daily maximum temperature exceeding the 90th percentile above the daily threshold for the reference period. The percentiles were calculated over a 31-day moving window within the preindustrial period (1850 to 1900). Hence, for a given day d, the threshold is the 90th percentile of the set of data A_d defined by

$$A_d = \bigcup_{y=1850}^{1900} \bigcup_{i=d-15}^{d+15} T_{y,i} \quad (6)$$

where $\bigcup$ denotes the union of sets, and $T_{y,i}$ is the daily maximum temperature day i in the year y. The daily magnitude (M_d) for each day of the heat wave is calculated as follows

$$M_d(T_d) = \begin{cases} \dfrac{T_d - T_{30y25p}}{T_{30y75p} - T_{30y25p}} \text{ if } T_d > T_{30y25p} \\ 0 \text{ if } T_d \leqslant T_{30y25p} \end{cases} \quad (7)$$

where T_d is the maximum daily temperature on day d of the heat wave, and T_{30y25p} and T_{30y75p} are the 25th and 75th percentile values, respectively, of the time series composed of 51-year annual maximum temperature within the preindustrial periods (1850 to 1900). For each year, HWMId is calculated as the sum of daily magnitudes over all consecutive days within a heat wave. An extreme heat wave is defined as the 99th percentile of the HWMId distribution over the historical periods (1850 to 2014) for each grid cell. A grid cell is considered exposed to an extreme heat wave in a given year if its HWMId exceeds this threshold (*37*, *38*).

Extreme events were calculated for land areas only. The global change in TXx was calculated as the average of all land areas, while extreme heat wave exposure was defined as the proportion of land area experiencing extreme heat waves relative to the total land area. For the 46 land subregions defined by the IPCC, TXx was calculated as the average of grid cells within each region, and extreme heat wave exposure was determined as the proportion of land area experiencing extreme heat waves relative to the total land area within each region. All extreme indices were calculated on the original grid of the CMIP6 GCMs.

OHC calculation

We compute annual-mean OHC (J m^{-2}) as follows

$$\mathrm{OHC} = \rho C_p \int_{z_1(x,y,z,t)}^{z_2(x,y,z,t)} \theta(x,y,z,t)\, dz \quad (8)$$

C_p is the specific heat capacity of seawater at 3990 J kg^{-1} c^{-1}, ρ is the density at 1025 kg m^{-3}, θ is the potential temperature, and z_1 and z_2 (m) are the depths of the bottom and surfaces for integration, respectively.

Assessment of aerosol differences between scenarios

To assess the potential influence of non-CO_2 forcing on the differences between the fast and slow scenarios, we quantified aerosol burdens using $PM_{2.5}$ (*42*). It is calculated from five aerosol components as $PM_{2.5}$ = sulfate aerosol (SO_4) + organic carbon (OA) + black carbon (BC) + 0.10 × dust (DU) + 0.25 × sea salt (SS). Monthly mean fields from the model level closest to the surface are used. This formula assumes that 100% of the BC, OA, and SO_4 is fine mode, whereas 25% of the sea salt and 10% of the dust are fine mode (*49*). To convert $PM_{2.5}$ from a mass mixing ratio to a concentration (units of μg m^{-3}), we multiply by air density, $\frac{PS}{TAS \times R_d} \times 10^9$, where PS is the surface pressure in pascals, TAS is the surface temperature in kelvin, and R_d is the dry gas constant equal to 287 J K^{-1} kg^{-1}.The number of models providing all aerosol components was restricted to 9 of the 29 models used in the manuscript, and the results of their MME were compared across two scenarios.

Statistical significance test

To assess the statistical significance of differences between the fast and slow scenarios, we used a two-step approach that distinguishes formal hypothesis testing from robustness assessment against model uncertainty. Statistical significance was assessed using a paired t test, which provides an explicit confidence-based test by accounting for the paired nature of model responses across scenarios.

In addition, to evaluate the robustness of the results to intermodel uncertainty, we applied a bootstrap-based resampling analysis following a previous study (*35*). For this analysis, the GMST,

Downloaded from https://www.science.org at EWHA Womans University on September 30, 2026

TXx, and extreme heat wave exposure values from the 29 CMIP6 models were randomly resampled with replacement to construct 10,000 realizations of their MME values for each scenario. In this resampling procedure, individual models could be selected multiple times. We then calculated the standard deviation of the bootstrap distributions for each scenario. Results were considered robust with respect to model uncertainty when the difference between the scenario means exceeded the sum of the bootstrapped standard deviations of the two scenarios.

This bootstrap-based criterion was not intended as a formal confidence interval or *P* value–based hypothesis test. Rather, it serves as a conservative filter to ensure that reported differences are not dominated by intermodel spread. Only results that were statistically significant according to the paired *t* test and additionally robust under the bootstrap resampling were highlighted and discussed.

Supplementary Materials

This PDF file includes:

Figs. S1 to S13
Table S1
References

REFERENCES

1. H. D. Matthews, N. P. Gillett, P. A. Stott, K. Zickfeld, The proportionality of global warming to cumulative carbon emissions. *Nature* **459**, 829–832 (2009).
2. M. R. Allen, D. J. Frame, C. Huntingford, C. D. Jones, J. A. Lowe, M. Meinshausen, N. Meinshausen, Warming caused by cumulative carbon emissions towards the trillionth tonne. *Nature* **458**, 1163–1166 (2009).
3. K. Zickfeld, M. Eby, H. D. Matthews, A. J. Weaver, Setting cumulative emissions targets to reduce the risk of dangerous climate change. *Proc. Natl. Acad. Sci. U.S.A.* **106**, 16129–16134 (2009).
4. M. Meinshausen, N. Meinshausen, W. Hare, S. C. B. Raper, K. Frieler, R. Knutti, D. J. Frame, M. R. Allen, Greenhouse-gas emission targets for limiting global warming to 2 °C. *Nature* **458**, 1158–1162 (2009).
5. C.-F. Schleussner, J. Rogelj, M. Schaeffer, T. Lissner, R. Licker, E. M. Fischer, R. Knutti, A. Levermann, K. Frieler, W. Hare, Science and policy characteristics of the Paris Agreement temperature goal. *Nat. Clim. Chang.* **6**, 827–835 (2016).
6. S. Fankhauser, S. M. Smith, M. Allen, K. Axelsson, T. Hale, C. Hepburn, J. M. Kendall, R. Khosla, J. Lezaun, E. Mitchell-Larson, M. Obersteiner, L. Rajamani, R. Rickaby, N. Seddon, T. Wetzer, The meaning of net zero and how to get it right. *Nat. Clim. Chang.* **12**, 15–21 (2022).
7. A. D. King, J. Peel, T. Ziehn, K. J. Bowen, H. L. O. McClelland, C. McMichael, Z. R. J. Nicholls, J. M. K. Sniderman, Preparing for a post-net-zero world. *Nat. Clim. Chang.* **12**, 775–777 (2022).
8. Y. Silvy, T. L. Frölicher, J. Terhaar, F. Joos, F. A. Burger, F. Lacroix, M. Allen, R. Bernardello, L. Bopp, V. Brovkin, J. R. Buzan, P. Cadule, M. Dix, J. Dunne, P. Friedlingstein, G. Georgievski, T. Hajima, S. Jenkins, M. Kawamiya, N. Y. Kiang, V. Lapin, D. Lee, P. Lerner, N. Mengis, E. A. Monteiro, D. Paynter, G. P. Peters, A. Romanou, J. Schwinger, S. Sparrow, E. Stofferahn, J. Tjiputra, E. Tourigny, T. Ziehn, AERA-MIP: Emission pathways, remaining budgets, and carbon cycle dynamics compatible with 1.5 and 2 °C global warming stabilization. *Earth Syst. Dyn.* **15**, 1591–1628 (2024).
9. J. Terhaar, T. L. Frölicher, M. T. Aschwanden, P. Friedlingstein, F. Joos, Adaptive emission reduction approach to reach any global warming target. *Nat. Clim. Chang.* **12**, 1136–1142 (2022).
10. J.-H. Oh, J.-S. Kug, S.-I. An, F.-F. Jin, M. J. McPhaden, J. Shin, Emergent climate change patterns originating from deep ocean warming in climate mitigation scenarios. *Nat. Clim. Chang.* **14**, 260–266 (2024).
11. S.-W. Yeh, S.-Y. Song, R. P. Allan, S.-I. An, J. Shin, Contrasting response of hydrological cycle over land and ocean to a changing CO_2 pathway. *NPJ Clim. Atmos. Sci.* **4**, 53 (2021).
12. T. F. Stocker, A. Schmittner, Influence of CO_2 emission rates on the stability of the thermohaline circulation. *Nature* **388**, 862–865 (1997).
13. P. M. Cox, M. S. Williamson, P. Friedlingstein, C. D. Jones, N. Raoult, J. Rogelj, R. M. Varney, Emergent constraints on carbon budgets as a function of global warming. *Nat. Commun.* **15**, 1885 (2024).
14. F. Lehner, A. W. Wood, J. A. Vano, D. M. Lawrence, M. P. Clark, J. S. Mankin, The potential to reduce uncertainty in regional runoff projections from climate models. *Nat. Clim. Chang.* **9**, 926–933 (2019).
15. L. J. Harrington, C.-F. Schleussner, F. E. L. Otto, Quantifying uncertainty in aggregated climate change risk assessments. *Nat. Commun.* **12**, 7140 (2021).
16. A. D. King, T. P. Lane, B. J. Henley, J. R. Brown, Global and regional impacts differ between transient and equilibrium warmer worlds. *Nat. Clim. Chang.* **10**, 42–47 (2020).
17. W. Zhang, T. Zhou, The effect of modeling strategies on assessments of differential warming impacts of 0.5°C. *Earths Future* **9**, e2020EF001640 (2021).
18. A. D. King, T. Ziehn, M. Chamberlain, A. R. Borowiak, J. R. Brown, L. Cassidy, A. J. Dittus, M. Grose, N. Maher, S. Paik, Exploring climate stabilisation at different global warming levels in ACCESS-ESM-1.5. *Earth Syst. Dyn.* **15**, 1353–1383 (2024).
19. A. D. King, A. R. Borowiak, J. R. Brown, D. J. Frame, L. J. Harrington, S. K. Min, A. Pendergrass, M. Rugenstein, J. K. Sniderman, D. A. Stone, Transient and quasi-equilibrium climate states at 1.5°C and 2°C global warming. *Earths Future* **9**, e2021EF002274 (2021).
20. Y.-H. Kim, S.-K. Min, N. P. Gillett, D. Notz, E. Malinina, Observationally-constrained projections of an ice-free Arctic even under a low emission scenario. *Nat. Commun.* **14**, 3139 (2023).
21. W. Weijer, W. Cheng, O. A. Garuba, A. Hu, B. Nadiga, CMIP6 models predict significant 21st century decline of the Atlantic meridional overturning circulation. *Geophys. Res. Lett.* **47**, e2019GL086075 (2020).
22. S. E. Perkins-Kirkpatrick, P. B. Gibson, Changes in regional heatwave characteristics as a function of increasing global temperature. *Sci. Rep.* **7**, 12256 (2017).
23. N. J. Leach, C. D. Roberts, M. Aengenheyster, D. Heathcote, D. M. Mitchell, V. Thompson, T. Palmer, A. Weisheimer, M. R. Allen, Heatwave attribution based on reliable operational weather forecasts. *Nat. Commun.* **15**, 4530 (2024).
24. J. Liu, H. Kim, M. Hashizume, W. Lee, Y. Honda, S. E. Kim, C. He, H. Kan, R. Chen, Nonlinear exposure-response associations of daytime, nighttime, and day-night compound heatwaves with mortality amid climate change. *Nat. Commun.* **16**, 635 (2025).
25. R. D. Lamboll, Z. R. J. Nicholls, C. J. Smith, J. S. Kikstra, E. Byers, J. Rogelj, Assessing the size and uncertainty of remaining carbon budgets. *Nat. Clim. Chang.* **13**, 1360–1367 (2023).
26. K. Zickfeld, M. Eby, H. D. Matthews, A. J. Weaver, Climate system responses to a common emission budget of carbon dioxide. *J. Climate* **29**, 2781–2800 (2016).
27. M. Leduc, H. D. Matthews, R. de Elía, Regional estimates of the transient climate response to cumulative CO_2 emissions. *Nat. Clim. Chang.* **6**, 474–478 (2016).
28. M. Chen, L. Chen, Y. Zhou, M. Hu, Y. Jiang, D. Huang, Y. Gong, Y. Xian, Rising vulnerability of compound risk inequality to ageing and extreme heatwave exposure in global cities. *NPJ Urban Sustain.* **3**, 38 (2023).
29. M. Meinshausen, Z. R. J. Nicholls, J. Lewis, M. J. Gidden, E. Vogel, M. Freund, U. Beyerle, C. Gessner, A. Nauels, N. Bauer, J. G. Canadell, J. S. Daniel, A. John, P. B. Krummel, G. Luderer, N. Meinshausen, S. A. Montzka, P. J. Rayner, S. Reimann, S. J. Smith, M. van den Berg, G. J. M. Velders, M. K. Vollmer, R. H. J. Wang, The shared socio-economic pathway (SSP) greenhouse gas concentrations and their extensions to 2500. *Geosci. Model Dev.* **13**, 3571–3605 (2020).
30. B. H. Samset, C. Zhou, J. S. Fuglestvedt, M. T. Lund, J. Marotzke, M. D. Zelinka, Earlier emergence of a temperature response to mitigation by filtering annual variability. *Nat. Commun.* **13**, 1578 (2022).
31. K. B. Tokarska, N. P. Gillett, Cumulative carbon emissions budgets consistent with 1.5 °C global warming. *Nat. Clim. Chang.* **8**, 296–299 (2018).
32. G. A. Meehl, C. A. Senior, V. Eyring, G. Flato, J.-F. Lamarque, R. J. Stouffer, K. E. Taylor, M. Schlund, Context for interpreting equilibrium climate sensitivity and transient climate response from the CMIP6 Earth system models. *Sci. Adv.* **6**, eaba1981 (2020).
33. I.-H. Park, S.-W. Yeh, W. Cai, G. Wang, S.-K. Min, S.-K. Lee, Present-day North Atlantic salinity constrains future warming of the Northern Hemisphere. *Nat. Clim. Chang.* **13**, 816–822 (2023).
34. F. J. M. M. Nijsse, P. M. Cox, M. S. Williamson, Emergent constraints on transient climate response (TCR) and equilibrium climate sensitivity (ECS) from historical warming in CMIP5 and CMIP6 models. *Earth Syst. Dynam.* **11**, 737–750 (2020).
35. W. Cai, G. Wang, B. Dewitte, L. Wu, A. Santoso, K. Takahashi, Y. Yang, A. Carréric, M. J. McPhaden, Increased variability of eastern Pacific El Niño under greenhouse warming. *Nature* **564**, 201–206 (2018).
36. X. Zhang, L. Alexander, G. C. Hegerl, P. Jones, A. K. Tank, T. C. Peterson, B. Trewin, F. W. Zwiers, Indices for monitoring changes in extremes based on daily temperature and precipitation data. *Wiley Interdiscip. Rev. Clim. Change* **2**, 851–870 (2011).
37. S. Lange, J. Volkholz, T. Geiger, F. Zhao, I. Vega, T. Veldkamp, C. P. Reyer, L. Warszawski, V. Huber, J. Jägermeyr, Projecting exposure to extreme climate impact events across six event categories and three spatial scales. *Earths Future* **8**, e2020EF001616 (2020).
38. W. Thiery, S. Lange, J. Rogelj, C.-F. Schleussner, L. Gudmundsson, S. I. Seneviratne, M. Andrijevic, K. Frieler, K. Emanuel, T. Geiger, Intergenerational inequities in exposure to climate extremes. *Science* **374**, 158–160 (2021).
39. I. M. Held, M. Winton, K. Takahashi, T. Delworth, F. Zeng, G. K. Vallis, Probing the fast and slow components of global warming by returning abruptly to preindustrial forcing. *J. Climate* **23**, 2418–2427 (2010).
40. T. L. Frölicher, M. Winton, J. L. Sarmiento, Continued global warming after CO_2 emissions stoppage. *Nat. Clim. Chang.* **4**, 40–44 (2014).

Downloaded from https://www.science.org at EWHA Womans University on September 30, 2026

41. K. von Schuckmann, M. D. Palmer, K. E. Trenberth, A. Cazenave, D. Chambers, N. Champollion, J. Hansen, S. A. Josey, N. Loeb, P. P. Mathieu, B. Meyssignac, M. Wild, An imperative to monitor Earth's energy imbalance. *Nat. Clim. Chang.* **6**, 138–144 (2016).
42. S. T. Turnock, R. J. Allen, M. Andrews, S. E. Bauer, M. Deushi, L. Emmons, P. Good, L. Horowitz, J. G. John, M. Michou, P. Nabat, V. Naik, D. Neubauer, F. M. O'Connor, D. Olivié, N. Oshima, M. Schulz, A. Sellar, S. Shim, T. Takemura, S. Tilmes, K. Tsigaridis, T. Wu, J. Zhang, Historical and future changes in air pollutants from CMIP6 models. *Atmos. Chem. Phys.* **20**, 14547–14579 (2020).
43. P. Wang, Y. Yang, D. Xue, L. Ren, J. Tang, L. R. Leung, H. Liao, Aerosols overtake greenhouse gases causing a warmer climate and more weather extremes toward carbon neutrality. *Nat. Commun.* **14**, 7257 (2023).
44. P. Friedlingstein, M. O'Sullivan, M. W. Jones, R. M. Andrew, J. Hauck, A. Olsen, G. P. Peters, W. Peters, J. Pongratz, S. Sitch, C. Le Quéré, J. G. Canadell, P. Ciais, R. B. Jackson, S. Alin, L. E. O. C. Aragão, A. Arneth, V. Arora, N. R. Bates, M. Becker, A. Benoit-Cattin, H. C. Bittig, L. Bopp, S. Bultan, N. Chandra, F. Chevallier, L. P. Chini, W. Evans, L. Florentie, P. M. Forster, T. Gasser, M. Gehlen, D. Gilfillan, T. Gkritzalis, L. Gregor, N. Gruber, I. Harris, K. Hartung, V. Haverd, R. A. Houghton, T. Ilyina, A. K. Jain, E. Joetzjer, K. Kadono, E. Kato, V. Kitidis, J. I. Korsbakken, P. Landschützer, N. Lefèvre, A. Lenton, S. Lienert, Z. Liu, D. Lombardozzi, G. Marland, N. Metzl, D. R. Munro, J. E. M. S. Nabel, S. I. Nakaoka, Y. Niwa, K. O'Brien, T. Ono, P. I. Palmer, D. Pierrot, B. Poulter, L. Resplandy, E. Robertson, C. Rödenbeck, J. Schwinger, R. Séférian, I. Skjelvan, A. J. P. Smith, A. J. Sutton, T. Tanhua, P. P. Tans, H. Tian, B. Tilbrook, G. van der Werf, N. Vuichard, A. P. Walker, R. Wanninkhof, A. J. Watson, D. Willis, A. J. Wiltshire, W. Yuan, X. Yue, S. Zaehle, Global carbon budget 2020. *Earth Syst. Sci. Data* **12**, 3269–3340 (2020).
45. C. P. Morice, J. J. Kennedy, N. A. Rayner, J. P. Winn, E. Hogan, R. E. Killick, R. J. H. Dunn, T. J. Osborn, P. D. Jones, I. R. Simpson, An updated assessment of near-surface temperature change from 1850: The HadCRUT5 data set. *J. Geophys. Res. Atmos.* **126**, e2019JD032361 (2021).
46. D. M. Lawrence, G. C. Hurtt, A. Arneth, V. Brovkin, K. V. Calvin, A. D. Jones, C. D. Jones, P. J. Lawrence, N. de Noblet-Ducoudré, J. Pongratz, S. I. Seneviratne, E. Shevliakova, The Land Use Model Intercomparison Project (LUMIP) contribution to CMIP6: Rationale and experimental design. *Geosci. Model Dev.* **9**, 2973–2998 (2016).
47. S. Fiedler, B. Stevens, M. Gidden, S. J. Smith, K. Riahi, D. van Vuuren, First forcing estimates from the future CMIP6 scenarios of anthropogenic aerosol optical properties and an associated Twomey effect. *Geosci. Model Dev.* **12**, 989–1007 (2019).
48. S. Russo, J. Sillmann, E. M. Fischer, Top ten European heatwaves since 1950 and their occurrence in the coming decades. *Environ. Res. Lett.* **10**, 124003 (2015).
49. J. Gomez, R. J. Allen, S. T. Turnock, L. W. Horowitz, K. Tsigaridis, S. E. Bauer, D. Olivié, E. S. Thomson, P. Ginoux, The projected future degradation in air quality is caused by more abundant natural aerosols in a warmer world. *Commun. Earth Environ.* **4**, 22 (2023).
50. D. H. Bi, M. Dix, S. Marsland, S. O'Farrell, A. Sullivan, R. Bodman, R. Law, I. Harman, J. Srbinovsky, H. A. Rashid, P. Dobrohotoff, C. Mackallah, H. L. Yan, A. Hirst, A. Savita, F. B. Dias, M. Woodhouse, R. Fiedler, A. Heerdegen, Configuration and spin-up of ACCESS-CM2, the new generation Australian Community Climate and Earth System Simulator Coupled Model. *J. South. Hemisph. Earth Syst. Sci.* **70**, 225–251 (2020).
51. T. Ziehn, M. A. Chamberlain, R. M. Law, A. Lenton, R. W. Bodman, M. Dix, L. Stevens, Y. P. Wang, J. Srbinovsky, The Australian Earth System Model: ACCESS-ESM1.5. *J. South. Hemisph. Earth Syst. Sci.* **70**, 193–214 (2020).
52. T. Semmler, S. Danilov, P. Gierz, H. F. Goessling, J. Hegewald, C. Hinrichs, N. Koldunov, N. Khosravi, L. J. Mu, T. Rackow, D. V. Sein, D. Sidorenko, Q. Wang, T. Jung, Simulations for CMIP6 With the AWI Climate Model AWI-CM-1-1. *J. Adv. Model. Earth Syst.* **12**, e2019MS002009 (2020).
53. T. W. Wu, Y. X. Lu, Y. J. Fang, X. G. Xin, L. Li, W. P. Li, W. H. Jie, J. Zhang, Y. M. Liu, L. Zhang, F. Zhang, Y. W. Zhang, F. H. Wu, J. L. Li, M. Chu, Z. Z. Wang, X. L. Shi, X. W. Liu, M. Wei, A. N. Huang, Y. C. Zhang, X. H. Liu, The Beijing Climate Center Climate System Model (BCC-CSM): The main progress from CMIP5 to CMIP6. *Geosci. Model Dev.* **12**, 1573–1600 (2019).
54. N. C. Swart, J. N. S. Cole, V. V. Kharin, M. Lazare, J. F. Scinocca, N. P. Gillett, J. Anstey, V. Arora, J. R. Christian, S. Hanna, Y. J. Jiao, W. G. Lee, F. Majaess, O. A. Saenko, C. Seiler, C. Seinen, A. Shao, M. Sigmond, L. Solheim, K. von Salzen, D. Yang, B. Winter, The Canadian Earth System Model version 5 (CanESM5.0.3). *Geosci. Model Dev.* **12**, 4823–4873 (2019).
55. G. Danabasoglu, J. F. Lamarque, J. Bacmeister, D. A. Bailey, A. K. DuVivier, J. Edwards, L. K. Emmons, J. Fasullo, R. Garcia, A. Gettelman, C. Hannay, M. M. Holland, W. G. Large, P. H. Lauritzen, D. M. Lawrence, J. T. M. Lenaerts, K. Lindsay, W. H. Lipscomb, M. J. Mills, R. Neale, K. W. Oleson, B. Otto-Bliesner, A. S. Phillips, W. Sacks, S. Tilmes, L. van Kampenhout, M. Vertenstein, A. Bertini, J. Dennis, C. Deser, C. Fischer, B. Fox-Kemper, J. E. Kay, D. Kinnison, P. J. Kushner, V. E. Larson, M. C. Long, S. Mickelson, J. K. Moore, E. Nienhouse, L. Polvani, P. J. Rasch, W. G. Strand, The Community Earth System Model Version 2 (CESM2). *J. Adv. Model. Earth Syst.* **12**, e2019MS001916 (2020).
56. A. Voldoire, D. Saint-Martin, S. Senesi, B. Decharme, A. Alias, M. Chevallier, J. Colin, J. F. Gueremy, M. Michou, M. P. Moine, P. Nabat, R. Roehrig, D. S. Y. Melia, R. Seferian, S. Valcke, I. Beau, S. Belamari, S. Berthet, C. Cassou, J. Cattiaux, J. Deshayes, H. Douville, C. Ethe, L. Franchisteguy, O. Geoffroy, C. Levy, G. Madec, Y. Meurdesoif, R. Msadek, A. Ribes, E. Sanchez-Gomez, L. Terray, R. Waldman, Evaluation of CMIP6 DECK Experiments With CNRM-CM6-1. *J. Adv. Model. Earth Syst.* **11**, 2177–2213 (2019).
57. R. Döscher, M. Acosta, A. Alessandri, P. Anthoni, T. Arsouze, T. Bergman, R. Bernardello, S. Boussetta, L.-P. Caron, G. Carver, M. Castrillo, F. Catalano, I. Cvijanovic, P. Davini, E. Dekker, F. J. Doblas-Reyes, D. Docquier, P. Echevarria, U. Fladrich, R. Fuentes-Franco, M. Gröger, J. v. Hardenberg, J. Hieronymus, M. P. Karami, J.-P. Keskinen, T. Koenigk, R. Makkonen, F. Massonnet, M. Ménégoz, P. A. Miller, E. Moreno-Chamarro, L. Nieradzik, T. van Noije, P. Nolan, D. O'Donnell, P. Ollinaho, G. van den Oord, P. Ortega, O. T. Prims, A. Ramos, T. Reerink, C. Rousset, Y. Ruprich-Robert, P. Le Sager, T. Schmith, R. Schrödner, F. Serva, V. Sicardi, M. S. Madsen, B. Smith, T. Tian, E. Tourigny, P. Uotila, M. Vancoppenolle, S. Wang, D. Wårlind, U. Willén, K. Wyser, S. Yang, X. Yepes-Arbós, Q. Zhang, The EC-Earth3 Earth system model for the Climate Model Intercomparison Project 6. *Geosci. Model Dev.* **15**, 2973–3020 (2022).
58. L. J. Li, Y. Q. Yu, Y. L. Tang, P. F. Lin, J. B. Xie, M. R. Song, L. Dong, T. J. Zhou, L. Liu, L. Wang, Y. Pu, X. L. Chen, L. Chen, Z. H. Xie, H. B. Liu, L. X. Zhang, X. Huang, T. Feng, W. P. Zheng, K. Xia, H. L. Liu, J. P. Liu, Y. Wang, L. H. Wang, B. H. Jia, F. Xie, B. Wang, S. W. Zhao, Z. P. Yu, B. W. Zhao, J. L. Wei, The Flexible Global Ocean-Atmosphere-Land System Model Grid-Point Version 3 (FGOALS-g3): Description and evaluation. *J. Adv. Model. Earth Syst.* **12**, e2019MS002012 (2020).
59. J. P. Dunne, L. W. Horowitz, A. J. Adcroft, P. Ginoux, I. M. Held, J. G. John, J. P. Krasting, S. Malyshev, V. Naik, F. Paulot, E. Shevliakova, C. A. Stock, N. Zadeh, V. Balaji, C. Blanton, K. A. Dunne, C. Dupuis, J. Durachta, R. Dussin, P. P. G. Gauthier, S. M. Griffies, H. Guo, R. W. Hallberg, M. Harrison, J. He, W. Hurlin, C. McHugh, R. Menzel, P. C. D. Milly, S. Nikonov, D. J. Paynter, J. Ploshay, A. Radhakrishnan, K. Rand, B. G. Reichl, T. Robinson, D. M. Schwarzkopf, L. T. Sentman, S. Underwood, H. Vahlenkamp, M. Winton, A. T. Wittenberg, B. Wyman, Y. Zeng, M. Zhao, The GFDL Earth System Model Version 4.1 (GFDL-ESM 4.1): Overall coupled model description and simulation characteristics. *J. Adv. Model. Earth Syst.* **12**, e2019MS002015 (2020).
60. M. Kelley, G. A. Schmidt, L. S. Nazarenko, S. E. Bauer, R. Ruedy, G. L. Russell, A. S. Ackerman, I. Aleinov, M. Bauer, R. Bleck, V. Canuto, G. Cesana, Y. Cheng, T. L. Clune, B. Cook, C. A. Cruz, A. D. Del Genio, G. S. Elsaesser, G. Faluvegi, N. Y. Kiang, D. Kim, A. A. Lacis, A. Leboissetier, A. N. LeGrande, K. K. Lo, J. Marshall, E. E. Matthews, S. McDermid, K. Mezuman, R. L. Miller, L. T. Murray, V. Oinas, C. Orbe, C. P. Garcia-Pando, J. P. Perlwitz, M. J. Puma, D. Rind, A. Romanou, D. T. Shindell, S. Sun, N. Tausnev, K. Tsigaridis, G. Tselioudis, E. S. Weng, J. B. Wu, M.-S. Yao, GISS-E2.1: Configurations and climatology. *J. Adv. Model. Earth Syst.* **12**, e2019MS002025 (2020).
61. K. D. Williams, D. Copsey, E. W. Blockley, A. Bodas-Salcedo, D. Calvert, R. Comer, P. Davis, T. Graham, H. T. Hewitt, R. Hill, P. Hyder, S. Ineson, T. C. Johns, A. B. Keen, R. W. Lee, A. Megann, S. F. Milton, J. G. L. Rae, M. J. Roberts, A. A. Scaife, R. Schiemann, D. Storkey, L. Thorpe, I. G. Watterson, D. N. Walters, A. West, R. A. Wood, T. Woollings, P. K. Xavier, The Met Office Global Coupled Model 3.0 and 3.1 (GC3.0 and GC3.1) configurations. *J. Adv. Model. Earth Syst.* **10**, 357–380 (2018).
62. A. A. Sellar, J. Walton, C. G. Jones, R. Wood, N. L. Abraham, M. Andrejczuk, M. B. Andrews, T. Andrews, A. T. Archibald, L. de Mora, H. Dyson, M. Elkington, R. Ellis, P. Florek, P. Good, L. Gohar, S. Haddad, S. C. Hardiman, E. Hogan, A. Iwi, C. D. Jones, B. Johnson, D. I. Kelley, J. Kettleborough, J. R. Knight, M. O. Kohler, T. Kuhlbrodt, S. Liddicoat, I. Linova-Pavlova, M. S. Mizielinski, O. Morgenstern, J. Mulcahy, E. Neininger, F. M. O'Connor, R. Petrie, J. Ridley, J. C. Rioual, M. Roberts, E. Robertson, S. Rumbold, J. Seddon, H. Shepherd, S. Shim, A. Stephens, J. C. Teixiera, Y. M. Tang, J. Williams, A. Wiltshire, P. T. Griffiths, Implementation of U.K. Earth system models for CMIP6. *J. Adv. Model. Earth Syst.* **12**, e2019MS001946 (2020).
63. E. M. Volodin, E. V. Mortikov, S. V. Kostrykin, V. Y. Galin, V. N. Lykossov, A. S. Gritsun, N. A. Diansky, A. V. Gusev, N. G. Iakovlev, A. A. Shestakova, S. V. Emelina, Simulation of the modern climate using the INM-CM48 climate model. *Russ. J. Numer. Anal. Math. Model.* **33**, 367–374 (2018).
64. E. M. Volodin, E. V. Mortikov, S. V. Kostrykin, V. Y. Galin, V. N. Lykossov, A. S. Gritsun, N. A. Diansky, A. V. Gusev, N. G. Iakovlev, Simulation of the present-day climate with the climate model INMCM5. *Climate Dynam.* **49**, 3715–3734 (2017).
65. O. Boucher, J. Servonnat, A. L. Albright, O. Aumont, Y. Balkanski, V. Bastrikov, S. Bekki, R. Bonnet, S. Bony, L. Bopp, P. Braconnot, P. Brockmann, P. Cadule, A. Caubel, F. Cheruy, F. Codron, A. Cozic, D. Cugnet, F. D'Andrea, P. Davini, C. de Lavergne, S. Denvil, J. Deshayes, M. Devilliers, A. Ducharne, J. L. Dufresne, E. Dupont, C. Ethe, L. Fairhead, L. Falletti, S. Flavoni, M. A. Foujols, S. Gardoll, G. Gastineau, J. Ghattas, J. Y. Grandpeix, B. Guenet, L. E. Guez, E. Guilyardi, M. Guimberteau, D. Hauglustaine, F. Hourdin, A. Idelkadi, S. Joussaume, M. Kageyama, M. Khodri, G. Krinner, N. Lebas, G. Levavasseur, C. Levy, L. Li, F. Lott, T. Lurton, S. Luyssaert, G. Madec, J. B. Madeleine, F. Maignan, M. Marchand, O. Marti, L. Mellul, Y. Meurdesoif, J. Mignot, I. Musat, C. Ottle, P. Peylin, Y. Planton, J. Polcher, C. Rio, N. Rochetin, C. Rousset, P. Sepulchre, A. Sima, D. Swingedouw, R. Thieblemont, A. K. Traore, M. Vancoppenolle, J. Vial, J. Vialard, N. Viovy, N. Vuichard, Presentation and evaluation of the IPSL-CM6A-LR climate model. *J. Adv. Model. Earth Syst.* **12**, e2019MS002010 (2020).
66. T. Hajima, M. Watanabe, A. Yamamoto, H. Tatebe, M. A. Noguchi, M. Abe, R. Ohgaito, A. Ito, D. Yamazaki, H. Okajima, A. Ito, K. Takata, K. Ogochi, S. Watanabe, M. Kawamiya,

Downloaded from https://www.science.org at EWHA Womans University on September 30, 2026

Development of the MIROC-ES2L Earth system model and the evaluation of biogeochemical processes and feedbacks. *Geosci. Model Dev.* **13**, 2197–2244 (2020).
67. H. Tatebe, T. Ogura, T. Nitta, Y. Komuro, K. Ogochi, T. Takemura, K. Sudo, M. Sekiguchi, M. Abe, F. Saito, M. Chikira, S. Watanabe, M. Mori, N. Hirota, Y. Kawatani, T. Mochizuki, K. Yoshimura, K. Takata, R. O'ishi, D. Yamazaki, T. Suzuki, M. Kurogi, T. Kataoka, M. Watanabe, M. Kimoto, Description and basic evaluation of simulated mean state, internal variability, and climate sensitivity in MIROC6. *Geosci. Model Dev.* **12**, 2727–2765 (2019).
68. W. A. Müller, J. H. Jungclaus, T. Mauritsen, J. Baehr, M. Bittner, R. Budich, F. Bunzel, M. Esch, R. Ghosh, H. Haak, T. Ilyina, T. Kleine, L. Kornblueh, H. Li, K. Modali, D. Notz, H. Pohlmann, E. Roeckner, I. Stemmler, F. Tian, J. Marotzke, A higher-resolution version of the Max Planck Institute Earth system model (MPI-ESM1. 2-HR). *J. Adv. Model. Earth Syst.* **10**, 1383–1413 (2018).
69. T. Mauritsen, J. Bader, T. Becker, J. Behrens, M. Bittner, R. Brokopf, V. Brovkin, M. Claussen, T. Crueger, M. Esch, I. Fast, S. Fiedler, D. Flaeschner, V. Gayler, M. Giorgetta, D. S. Goll, H. Haak, S. Hagemann, C. Hedemann, C. Hohenegger, T. Ilyina, T. Jahns, D. Jimenez-de-la-Cuesta, J. Jungclaus, T. Kleinen, S. Kloster, D. Kracher, S. Kinne, D. Kleberg, G. Lasslop, L. Kornblueh, J. Marotzke, D. Matei, K. Meraner, U. Mikolajewicz, K. Modali, B. Mobis, W. A. Muller, J. E. M. S. Nabel, C. C. W. Nam, D. Notz, S. S. Nyawira, H. Paulsen, K. Peters, R. Pincus, H. Pohlmann, J. Pongratz, M. Popp, T. J. Raddatz, S. Rast, R. Redler, C. H. Reick, T. Rohrschneider, V. Schemann, H. Schmidt, R. Schnur, U. Schulzweida, K. D. Six, L. Stein, I. Stemmler, B. Stevens, J. S. von Storch, F. X. Tian, A. Voigt, P. Vrese, K. H. Wieners, S. Wilkenskjeld, A. Winkler, E. Roeckner, Developments in the MPI-M Earth System Model version 1.2 (MPI-ESM1.2) and its response to increasing CO_2. *J. Adv. Model. Earth Syst.* **11**, 998–1038 (2019).
70. S. Yukimoto, H. Kawai, T. Koshiro, N. Oshima, K. Yoshida, S. Urakawa, H. Tsujino, M. Deushi, T. Tanaka, M. Hosaka, S. Yabu, H. Yoshimura, E. Shindo, R. Mizuta, A. Obata, Y. Adachi, M. Ishii, The Meteorological Research Institute Earth System Model Version 2.0, MRI-ESM2.0: Description and basic evaluation of the physical component. *J. Meteorol. Soc. Jpn.* **97**, 931–965 (2019).
71. J. Cao, B. Wang, Y. M. Yang, L. B. Ma, J. Li, B. Sun, Y. Bao, J. He, X. Zhou, L. G. Wu, The NUIST Earth System Model (NESM) version 3: Description and preliminary evaluation. *Geosci. Model Dev.* **11**, 2975–2993 (2018).
72. O. Seland, M. Bentsen, D. Olivie, T. Toniazzo, A. Gjermundsen, L. S. Graff, J. B. Debernard, A. K. Gupta, Y. C. He, A. Kirkevag, J. Schwinger, J. Tjiputra, K. S. Aas, I. Bethke, Y. C. Fan, J. Griesfeller, A. Grini, C. C. Guo, M. Ilicak, I. H. H. Karset, O. Landgren, J. Liakka, K. O. Moseid, A. Nummelin, C. Spensberger, H. Tang, Z. S. Zhang, C. Heinze, T. Iversen, M. Schulz, Overview of the Norwegian Earth System Model (NorESM2) and key climate response of CMIP6 DECK, historical, and scenario simulations. *Geosci. Model Dev.* **13**, 6165–6200 (2020).
73. Y.-C. Wang, H.-H. Hsu, C.-A. Chen, W.-L. Tseng, P.-C. Hsu, C.-W. Lin, Y.-L. Chen, L.-C. Jiang, Y.-C. Lee, H.-C. Liang, W.-M. Chang, W.-L. Lee, C.-J. Shiu, Performance of the Taiwan Earth system model in simulating climate variability compared with observations and CMIP6 model simulations. *J. Adv. Model. Earth Syst.* **13**, e2020MS002353 (2021).

Acknowledgments
Funding: This work was supported by the following: National Research Foundation of Korea (NRF) grant funded by the Korea government (Ministry of Science and ICT, MSIT) (RS-2024-00335725) (to I.-H.P.) and Korea Environment Industry and Technology Institute (KEITI) through the Climate Change R&D Project for New Climate Regime funded by the Korea Ministry of Environment (MOE) (2022003560001) (to S.-W.Y.). **Author contributions:** Conceptualization: I.-H.P. and S.-W.Y. Methodology: I.-H.P. and S.-W.Y. Investigation: I.-H.P. and S.-W.Y. Formal analysis: I.-H.P. Data curation: I.-H.P. Software: I.-H.P. Validation: I.-H.P. Visualization: I.-H.P. Resources: I.-H.P. Funding acquisition: I.-H.P. Project administration: I.-H.P. Supervision: S.-W.Y. and A.D.K. Writing—original draft: I.-H.P. and S.-W.Y. Writing—review and editing: I.-H.P., S.-W.Y., and A.D.K. **Competing interests:** The authors declare that they have no competing interests. **Data, code, and materials availability:** All data and code needed to evaluate and reproduce the results in the paper are present in the paper and/or the Supplementary Materials. The data for this study are available from https://doi.org/10.5281/zenodo.18629510. This study did not generate new materials.

Submitted 20 September 2025
Accepted 31 March 2026
Published 29 April 2026
10.1126/sciadv.aec4566

Downloaded from https://www.science.org at EWHA Womans University on September 30, 2026

ScienceAdvances

The pace of meeting carbon emission targets alters regional climate risks

In-Hong Park, Sang-Wook Yeh, and Andrew D. King

Sci. Adv. **12** (18), eaec4566. DOI: 10.1126/sciadv.aec4566

View the article online
https://www.science.org/doi/10.1126/sciadv.aec4566
Permissions
https://www.science.org/help/reprints-and-permissions

Downloaded from https://www.science.org at EWHA Womans University on September 30, 2026

Use of this article is subject to the Terms of service

Science Advances (ISSN 2375-2548) is published by the American Association for the Advancement of Science. 1200 New York Avenue NW, Washington, DC 20005. The title *Science Advances* is a registered trademark of AAAS.

Copyright © 2026 The Authors, some rights reserved; exclusive licensee American Association for the Advancement of Science. No claim to original U.S. Government Works. Distributed under a Creative Commons Attribution NonCommercial License 4.0 (CC BY-NC).